Faraday Discussions

Cite this: DOI: 10.1039/d5fd00118h

ROYAL SOCIETY OF CHEMISTRY

PAPER

View Article Online
View Journal

Unravelling the role of additives in the structure of non-aqueous media at the electrode surface under potential control

Nathaniel J. D. Hill, [abc] Ciarán O'Brien, *[acd] Paul M. Donaldson, [c] Hansaem Jang, [a] Bhavin Siritanaratkul, [a] Gilberto Teobaldi, [d] Alexander J. Cowan *[a] and Adrian M. Gardner *[ab]

Received 19th November 2025, Accepted 16th December 2025
DOI: 10.1039/d5fd00118h

Efficiency and selectivity of electrochemical reactions are controlled by micro-environments within the electric double layer (EDL) at the electrode–electrolyte interface. In electrocatalysis, additives can direct the interfacial structure, enhancing activities. Our current level of understanding of the fundamental interactions between the solvent, the electrolyte, and additives at the electrode surface under potential control are limited. This makes *a priori* predictions of the EDL structure challenging. Vibrational Sum Frequency Generation (VSFG) spectroscopy allows for observation of interface-specific vibrational signatures from which interfacial species may be identified and their orientation determined, providing a way to study the fundamental behaviour of electrified interfaces. We exploit this to study the structure of acetonitrile (CH_3CN) in the presence of H_2O and *N*-methyl-2-pyrrolidone (NMP) at a gold electrode under potential control. At low concentrations of H_2O (300 ppm), the VSFG signatures of CH_3CN are weak and become increasingly apparent as the concentration of H_2O increases. We conclude that this is a result of the formation of an interfacial layer with increased net ordering of CH_3CN molecules due to hydrogen bonding with H_2O disrupting the microstructured CH_3CN environment. At low concentrations of H_2O, NMP accumulates at the negatively charged electrode surface, disrupting the CH_3CN structure; however, addition of H_2O perturbs the NMP structure, leading to an ordered CH_3CN interfacial layer being formed.

[a]*Stephenson Institute for Renewable Energy (SIRE), Department of Chemistry, University of Liverpool, Liverpool L69 7ZF, UK. E-mail: acowan@liverpool.ac.uk; ciaran.o-brien2@liverpool.ac.uk*

[b]*Early Career Laser Laboratory and Surface Science Research Centre, University of Liverpool, Liverpool L69 3BX, UK. E-mail: adrian.gardner@liverpool.ac.uk*

[c]*Central Laser Facility, Research Complex at Harwell, STFC-Rutherford Appleton Laboratory, Harwell Campus, Didcot OX11 0QX, UK*

[d]*Scientific Computing Department, Rutherford Appleton Laboratory, STFC UKRI, Harwell Campus, Didcot OX11 0QX, UK*

Open Access Article. Published on 16 December 2025. Downloaded on 5/22/2026 4:03:50 AM.
This article is licensed under a Creative Commons Attribution 3.0 Unported Licence.

Open Access Article. Published on 16 December 2025. Downloaded on 5/22/2026 4:03:50 AM.
This article is licensed under a Creative Commons Attribution 3.0 Unported Licence.

1. Introduction

Electron transfer processes between heterogeneous media are fundamental to electrochemical devices applied to energy storage and conversion, or chemical synthesis.[1–3] The efficiency and selectivity of these electrochemical reactions depend greatly on the micro-environments within the electric double layer (EDL) at the electrode–electrolyte interface.[4] The structure and composition of the interface are dependent on many factors, including local solvation structures, charge distribution, specific surface sites, surface coverage, and the local electric field.[5–10] These factors influence electrochemical reactions, directing competitive processes to favour one pathway over another. Aqueous electrode–electrolyte interfaces are the most widely studied. Alternative solvents with wider electrochemical windows allow devices to access energetically unfavourable redox chemistries with reduced faradaic competition from solvent redox reactions (*e.g.* hydrogen evolution from H_2O). Applications such as ammonia synthesis, lithium–metal batteries, and lithium–air batteries become accessible with sufficiently wide electrochemical windows.[11–14] One of the challenges for electrocatalytic CO_2 reduction (CO_2R) is to suppress the competing water reduction to improve the faradaic efficiency. Acetonitrile (CH_3CN), the focus of this work, is a common non-aqueous solvent. Its relatively high dielectric constant is compatible with a wide range of supporting electrolyte salts.[15] It is a weak Brønsted acid and Lewis base, allowing it to interact with interfacial species in different ways.[16] The solvent reduction potential of acetonitrile is more negative than that of H_2O and hence is thought not to compete with the desired reductive reactions, although intermolecular interactions (*e.g.* hydrogen bonding) are altered.[9,17–20] Additives can be introduced to direct the structure and composition of the interfacial environment to promote desired pathways. For example, it has been shown that adding small amounts of *N*-methyl-2-pyrrolidone (NMP) can perturb the EDL structure, resulting in activation of a molecular catalyst for CO_2R at less negative potentials.[21–23] Owing to the natural hygroscopicity of acetonitrile, contamination from ambient water is likely, introducing an amphiprotic, polar, electrochemically active additive to the system. Small amounts of water in acetonitrile have been seen to enhance CO_2R.[9,24] However, an understanding of the fundamental interactions of NMP or H_2O with the other species at the interface, which leads to these observations, is lacking, precluding rational design of electrolyte composition.

Metrics for device performance, including product quantification, current–voltage profiles, and electrochemical techniques, can provide some insights into some interface properties, *e.g.* capacitance and electrochemical stripping. However, these methods lack the information required for developing predictive models of the interface.[25] Determining the entire EDL composition and structure by simulation is beyond state-of-the-art computational methodologies and requires development of complex models of the double layer under potentiostatic control that include interactions between explicit solvent, electrolyte ions, additives, and the charged electrode surface.[26–28] It is therefore important to employ and develop surface-sensitive techniques that can probe electrochemical interfaces under potential control. When performed on well-controlled systems, these

Open Access Article. Published on 16 December 2025. Downloaded on 5/22/2026 4:03:50 AM.
This article is licensed under a Creative Commons Attribution 3.0 Unported Licence.

studies can be used to advance our understanding of the EDL and improve *in silico* techniques.

Surface-sensitive vibrational spectroscopy, when coupled with potentiostatic control, allows the potential-dependent vibrational signatures of species within the EDL to be observed. These spectroscopic signatures provide insight into the changing composition of the EDL and provide mechanistic understanding of redox reactions. Vibrational frequencies are also sensitive to the environment and hence can be used to provide insight into the interactions within the changing interfacial environment. Here we use Vibrational Sum Frequency Generation (VSFG) spectroscopy. The detailed principles of VSFG,[29,30] and experimental application of VSFG to electrochemical interfaces,[31,32] are presented elsewhere. VSFG is highly surface specific, making it a powerful tool for observing (buried) electrochemical interfaces. In VSFG, a high-intensity mid-infrared (MIR) electric field induces a coherent polarisation at the interface, which is probed, in our case, by a high-intensity near-infrared (NIR) electric field, producing a low-intensity field at the sum of the frequencies of the MIR and NIR electric fields. The charge of the (polarised) electrode surface is effectively screened by the high-dielectric (solvated) supporting electrolyte salts which accumulate at the electrode surface; this results in the generation of large electric (DC) fields within the EDL. As a result, VSFG is sensitive to the whole EDL.[31,32]

Here, we operate in a 'backside' geometry, so-called because the optical electric fields are propagated through the backside of a thin-film electrode (Fig. 1a and b), as has been previously demonstrated.[33–36] This configuration has several advantages: bulk electrolyte dynamics are not constrained, infrared attenuation from

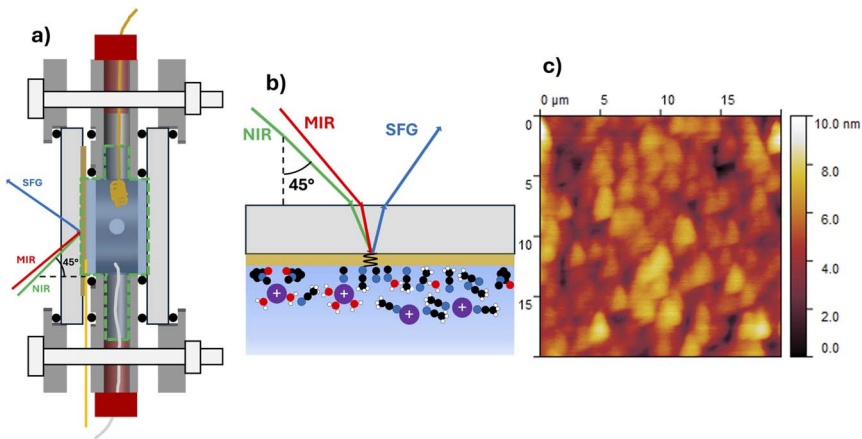

Fig. 1 (a) A cross section of the electrochemical cell: the body pieces of the cell (dark grey, polyether ether ketone), CaF_2 windows, and NBR O-rings (black) are compressed by bolts and nuts (white), creating a sealed bulk-electrolyte volume (green dotted). The gold counter electrode (gold) and silver reference electrode (silver) are brought into the side of the cell through septa (red). The incident and generated beams are transmitted through the backside of the thin-film electrode (dark gold). The electrode is connected to the external circuit *via* a piece of gold foil (yellow). (b) An illustrative representation of the spectroscopic geometry at the window and electrode–electrolyte interface, with possible EDL species. (c) Atomic force microscopy image of the surface morphology of a pristine Au electrode.

Open Access Article. Published on 16 December 2025. Downloaded on 5/22/2026 4:03:50 AM. This article is licensed under a Creative Commons Attribution 3.0 Unported Licence.

the bulk electrolyte is alleviated, and the effects of gas evolution are reduced. Thin (~10–40 nm) electrodes can exhibit nano-to-micrometer structuring (Fig. 1c). It has been demonstrated that nanostructured materials can enhance electric fields at the interface through surface plasmon resonances, leading to improved signal-to-noise ratios in the spectra obtained at electrochemically resilient electrode surfaces under operational conditions.[35,37–39]

Surface Enhanced Raman Spectroscopy (SERS), and Surface Enhanced Infrared Absorption Spectroscopy (SEIRAS) have been used to study the potential-dependent structure and decomposition of acetonitrile at gold surfaces.[14,40,41] In these studies, the expected orientation of acetonitrile molecules close to the electrode surface was explained with simple electrostatic arguments treating the electrode surface as a polarised charge.[14,41] It was reported that the dipole moment of CH_3CN orientates antiparallel to the DC field, E_{DC}, within the EDL, *e.g.* CH_3CN molecules are oriented with the positive CH_3 group pointing towards a negatively charged electrode surface. We extend these studies by probing the potential-dependent interfacial composition and orientation of acetonitrile at a gold electrode in electrolytes containing differing H_2O concentrations and the non-aqueous additive, NMP. Density functional theory (DFT) and *ab initio* molecular dynamics (AIMD) aid spectral assignments and deepen the understanding of the local interfacial environments. We show that the interfacial electric field and CH_3CN structure is modulated by the presence of H_2O. Under "dry" conditions, NMP accumulates at the Au surface as the electrode is increasingly negatively polarised. We show that the orientation of interfacial species is strongly controlled by dispersive interactions and successfully predict preferentially adsorbed species *in silico*.

2. Methods

2.1. Materials

Acetonitrile (CH_3CN, 99.8% anhydrous), 1-methyl-2-pyrrolidone (NMP, 99.5% anhydrous), tetrabutylammonium hexafluorophosphate (TBA PF_6, 99.0%), were all purchased from Merck.

2.2. Au thin-film electrode preparation

CaF_2 polished windows of 2 mm thickness (IR-grade, Crystran) were cleaned with ethanol, rinsed with deionised water (18.2 MΩ cm; direct-Q 3 UV, Merck) and dried under a stream of nitrogen. Gold (99.95%, Advent Research Materials) was deposited by thermal deposition at 6×10^{-6} mbar at a rate of 0.1 ± 0.05 Å s^{-1} to a thickness of approximately 25 nm determined *in situ* by a quartz crystal microbalance (see Note 1.2 in the SI).

2.3. Electrolyte preparation

We studied five electrolytes comprising CH_3CN and ~0.1 M $TBAPF_6$: (i) Molecular-sieve-dried acetonitrile (3 Å, 48 hours) and $TBAPF_6$ (2×10^{-2} mbar, 20 hours), denoted "dry" (300 ppm H_2O). (ii) A solution prepared under atmospheric lab conditions, denoted "undried" (2100 ppm H_2O). (iii) 2% (by volume) water was added to the undried solution, denoted "wet" (24 000 ppm H_2O). (iv) "Dry" and (v) "wet" NMP-containing electrolytes, with H_2O contents of 430 and 25 000 ppm,

 This journal is © The Royal Society of Chemistry 2026

respectively, were made by adding 10% (by volume) molecular-sieve-dried NMP (3 Å, 48 hours) to the "dry" or "wet" acetonitrile solutions. Water content was measured by Karl–Fischer titration after spectroelectrochemical experiments.

2.4. VSFG cell design

The VSFG cell, outlined in Fig. 1a, has been described elsewhere.[42] The counter electrode, 0.5 mm diameter gold wire (99.95%, Advent Research Materials), and silver pseudo-reference wire (99.99%, Advent Research Materials), were polished with P1200 SiC sandpaper and rinsed with deionized water (18.2 MΩ cm; direct-Q 3 UV, Merck).

2.5. VSFG experiments

The VSFG spectrometer has been recently described elsewhere.[21,42,43] Briefly, near-IR (1030 nm, 10 kHz, ~1.5 ps, ~13 cm^{-1} line width, ~45° angle of incidence, ~57 mW, 600 μm FWHM) and mid-IR (10 kHz, 170 fs, ~150 cm^{-1} at 2160 cm^{-1}, ~50° angle of incidence, ~22 mW, 400 μm ($1/e^2$)) laser pulses were overlapped at the sample (Fig. 1b). The generated SFG signal was relayed to a spectrograph (Andor, Kymera) before being detected on a CCD camera (Andor, iDus416). All experiments employed a ppp polarisation combination. For experiments where no salt or solvent drying was carried out, the cell was assembled, filled and purged with Ar (99.998%, BOC). Where dried salt and solvent were used, the cell components were dried at 40 °C for at least 12 h, before being assembled and brought into an Ar-filled glovebox to be filled and sealed. All spectra reported in the main text are obtained under chronoamperometric control for no longer than 610 s per potential step (Fig. S15 and S16). The ordering of the potential-dependent experiments were carefully controlled – see Note 1.1 in the SI.

2.6. AFM electrode characterisation

AFM was performed on an electrode prepared as described above, using a contact-mode cantilever (Pointprobe®, NanoWorld®, Switzerland) on an AFM nose cone (Keysight Technologies, United States). This nose cone was loaded into an atomic force microscope (5500 AFM, Keysight Technologies, United States) with beam-bounce detection of cantilever deflection. Once the cantilever was positioned, images were obtained using Keysight NanoNavigator software (version 1.8.2), and the morphologies were analysed using Gwyddion (version 2.61).

2.7. Simulation parameters

All DFT calculations were performed in the Projector-Augmented Wave (PAW) approach with the VASP 6.3.2 code using a plane-wave basis set with periodic boundary conditions.[44,45] VASPsol++ was used to introduce implicit solvent to the simulation cell to screen charge and impose a constant potential constraint on the calculations (implicit solvent parameters given in the SI, Table S5).[46] The chemical potential imposed by the VASPsol++ solvent was referenced to the potential of the standard hydrogen electrode *via* a calculation of the Gibbs free energy difference of the ferrocene/ferrocenium couple in the implicit solvent phase (details given in the SI, Table S6). The PBE approximation to the exchange–correlation functional was used alongside Grimme's D3 van der Waals

Open Access Article. Published on 16 December 2025. Downloaded on 5/22/2026 4:03:50 AM. This article is licensed under a Creative Commons Attribution 3.0 Unported Licence.

Open Access Article. Published on 16 December 2025. Downloaded on 5/22/2026 4:03:50 AM.
This article is licensed under a Creative Commons Attribution 3.0 Unported Licence.

correction.[47,48] A patch was applied to the dispersion correction routines in the manner of Sakong and Groβ,[49] which omitted pairwise Au–Au D3 forces, as well as all D3 energies, in all but the atoms in the top layer of the gold surface and the adsorbate atoms. Details of the computational methodology are expanded upon in the SI, Section 3.

Molecular dynamics in the NVT ensemble were used to obtain power spectra for CH_3CN (timestep = 0.75 fs, SCF tolerance = 10^{-4} eV, 2 × 2 × 1 Γ-centered *k*-point mesh, using a Nosé–Hoover thermostat with the "SMASS" parameter set to obtain a thermostat oscillation period of approximately 80 fs).[50] Trajectories were run for a minimum of 2 ps, and initialized with displacements and velocities calculated to result in a statistically correct distribution of harmonic modes at 300 K, in the manner of West and Estreicher.[51] Trajectory analyses and power spectra calculations were performed using TRAVIS.[52–54] All geometry construction was performed using the Atomic Simulation Environment libraries.[55]

3. Results and discussion

The potential-dependent VSFG spectra obtained for CH_3CN in the 2000–2300 cm^{-1} range are shown in Fig. 2. For ease of discussion, we separate this wavenumber range into four regions denoted as CN3, CN2, CN1 and AN, based on our assignments discussed below. We employ a delay between the broadband MIR pulse and the narrowband time-asymmetric NIR pulse; this effectively suppresses the large non-resonant signal of the Au interface.[56] We use a consistent delay throughout the main text (800 fs), comparing spectra obtained at other delays (0, 200, 400, 600, 800 and 1000 fs) in the SI, Fig. S1–S3 and S5–S13. The relative intensity of features in VSFG spectra are dependent on the MIR laser spectral profile. The result is that comparisons of the relative intensities of features observed in the VSFG spectra do not give any indication of relative

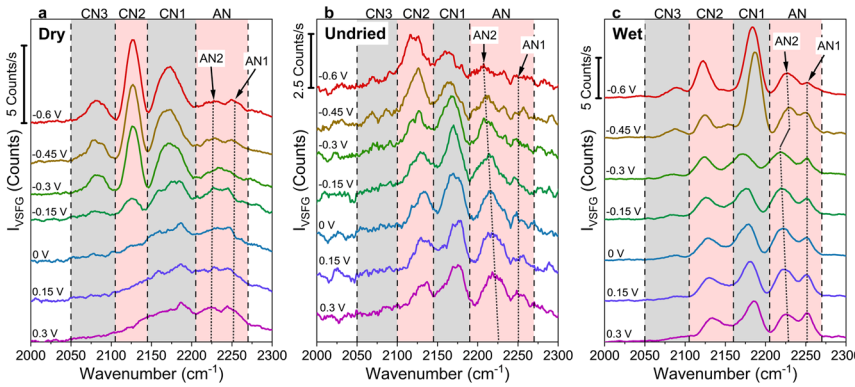

Fig. 2 VSFG spectra in the 2000–2300 cm^{-1} region as a function of applied bias *vs.* Ag wire for (a) dry, (b) undried, and (c) wet acetonitrile/0.1 M $TBAPF_6$ solutions, obtained during chronoamperometry. Signals were taken with an 800 fs delay of the NIR pulse. Traces have been offset for clarity. Several spectral regions, denoted AN, CN1, CN2 and CN3, and two specific bands denoted AN1 and AN2, have been highlighted to facilitate discussion.

Open Access Article. Published on 16 December 2025. Downloaded on 5/22/2026 4:03:50 AM.
This article is licensed under a Creative Commons Attribution 3.0 Unported Licence.

populations or net ordering of the different species at the interface; however, the potential-dependent intensities of each feature are insightful.

3.1. Effect of H_2O on interfacial CH_3CN structure

Potential-dependent VSFG spectra of dry electrolyte (300 ppm H_2O) are shown in Fig. 2a. At +0.0 V (hereinafter, all potentials are referenced *vs.* Ag wire unless explicitly stated) show four positive-going bands, with peak positions at ~2235, 2175, 2125 and 2080 cm^{-1}, superimposed on a broad baseline. The broad baseline is assigned to residual non-resonant signal observed at this time-delay. Closer inspection of the broad band within the AN spectral region at ~2235 cm^{-1} of the dry solution shows it has a strongly potential-dependent shape, and it appears to be composed of two bands with peak positions at ~2250 and 2225 cm^{-1}, denoted AN1 and AN2, respectively, and are most clearly observed at +0.3 and −0.6 V. The AN2 band is observed more clearly with both the undried and wet electrolytes (Fig. 2b and c, respectively). The AN1 band is only weakly observed in the undried spectra, most notably at the most-positive potentials studied, whereas, in the wet electrolyte, AN1 is present at all potentials studied – we return to this below. The wavenumber of AN1 is in excellent agreement with the solution-phase vibrational band of pure CH_3CN, as well as that of CH_3CN as a 0.1 M $TBAPF_6$ solution (Fig. S14b). We therefore assign AN1 to interfacial CH_3CN. To be VSFG-active, the environment must show net ordering, hence these CH_3CN molecules must lie within the interfacial region ordered by the charged electrode surface. In bulk CH_3CN solution, the CN-stretching vibration is in Fermi resonance with a combination band of the CC-stretch and the CH_3 deformation;[57] the band at ~2250 cm^{-1} is assigned to the component with predominantly CN-stretching character. A significantly weaker band is observed in the solution-phase FTIR spectrum at ~2292 cm^{-1} and assigned to the component with predominately combination-band character. Owing to the low strength of this transition, combined with the low MIR intensity at this wavenumber, this band is not clearly observed in the VSFG spectra.

In the AN spectral region, only one vibrational mode for solution-phase CH_3CN is observed in the harmonic DFT calculations: the CN fundamental stretch. The calculated wavenumber of this mode is dependent on the local environment (Fig. 3a). It is stressed that all calculations in this work make use of the Born–Oppenheimer approximation, and so will not account for the Fermi resonance interaction, which requires treatment of nuclear quantum dynamics.[58] We highlight that the local environment will perturb ν(CN) of CH_3CN by both altering the fundamental vibrational wavenumber and through modifying the Fermi resonance interaction. Given the strong dependency of environment and orientation on the calculated vibrational wavenumber, we explored the model interface using AIMD. The power spectrum of each trajectory analysed for the construction of Fig. 3b used only the position data of the CN group of the CH_3CN molecule. A full CH_3CN power spectrum of each system in Fig. 3b is shown in Fig. S22. For the power spectra calculated from models containing a surface, the line shape becomes complicated. Interaction with the surface and the local field of the tumbling CH_3CN molecule results in a broadened distribution of vibrational levels in this wavenumber range, notably at lower wavenumber than bulk CH_3CN, as predicted by the harmonic calculation of physisorbed CH_3CN in Fig. 3a. These

Open Access Article. Published on 16 December 2025. Downloaded on 5/22/2026 4:03:50 AM.
This article is licensed under a Creative Commons Attribution 3.0 Unported Licence.

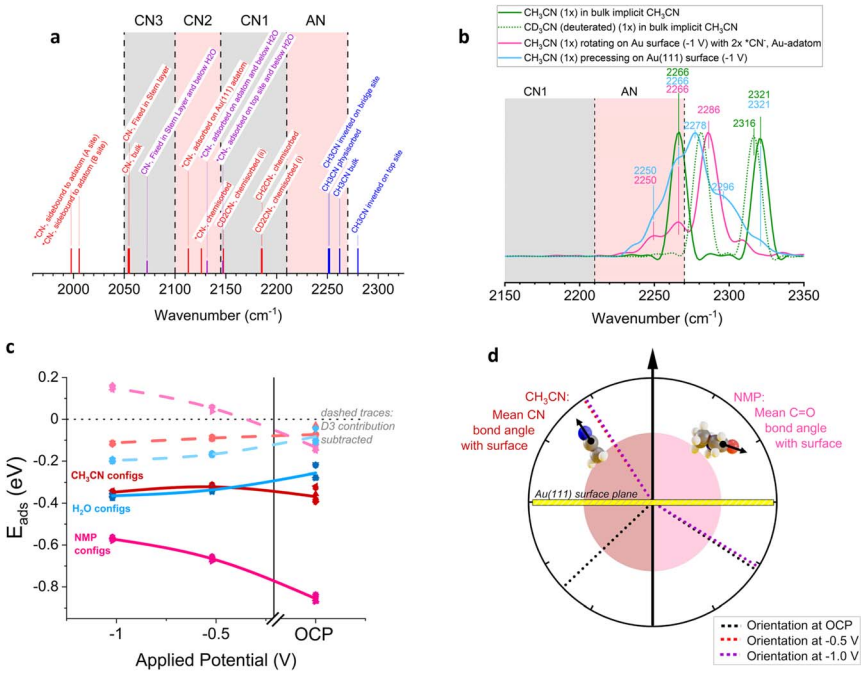

Fig. 3 (a) Harmonic vibrational wavenumbers calculated with DFT, modelled in VAS-Psol++ implicit CH_3CN + 0.1 M electrolyte. Where gold surfaces are present in these models, a strong negative potential is applied; electron density is held to a potential of *ca.* −1.0 V *vs.* SHE (E_{Fermi} = −3.5 eV). The data is grouped into CH_3CN-containing models (blue labels), models containing breakdown products of CH_3CN (red labels) and models containing breakdown products coordinated to H_2O (purple labels). Frequencies are scaled by a constant chosen to match the CN stretch in bulk CD_3CN to its experimental value.[56] (b) Power spectra (Fourier transforms of the mass-weighted velocity autocorrelation functions) of the CN group of a single CH_3CN molecule from VASP DFT-MD trajectories for a selection of CH_3CN environments in the experimentally observed ν(CN) region. (c) Mean calculated adsorption energies (in eV) for a sample of CH_3CN (red), NMP (pink) and water (blue) configurations on Au(111), plotted against applied potential, from open-circuit potential (OCP, no external potential applied) to −1.0 V *vs.* SHE. Trend lines are drawn through the mean of each dataset at each potential level. The adsorption energies are also plotted without the semi-empirical D3 van der Waals contribution for both series (accompanied by dashed lines). (d) Mean elevation angle of the adsorbate with the gold surface illustrating orientation of the relaxed structures of CH_3CN and NMP sampled in (c), as represented by projections of the unit vector of the nitrile group bond in CH_3CN on Au(111), and the unit vector of the carbonyl group bond in NMP.

results are qualified by limitations discussed in detail in Note 1.5 of the SI. We propose that, due to the redshifted frequency and the broad distribution of vibrational levels of our AIMD calculations, the broad AN2 band observed in the VSFG spectra should be assigned to CH_3CN interacting with the Au surface.

To develop an understanding of potential-dependent surface behaviour, we calculated the orientation of CH_3CN at OCP, −0.5 V and −1.0 V (*vs.* SHE) (Fig. 3d). CH_3CN is predicted to orient with the nitrogen atom pointed towards the Au electrode at OCP, with the nitrogen atom pointing away from the Au electrode at −0.5 V through to −1.0 V, though the CN bond is not calculated to orientate

Open Access Article. Published on 16 December 2025. Downloaded on 5/22/2026 4:03:50 AM. This article is licensed under a Creative Commons Attribution 3.0 Unported Licence.

perpendicularly to the Au surface at any potential. This is consistent with the potential-dependent shape of the AN1/2 bands in the VSFG spectra of the dry electrolyte (Fig. 2a) discussed above, which, notably, is not apparent for the undried and wet electrolytes. The calculated adsorption energy of CH_3CN on the model Au(111) surface, with and without the semi-empirical D3 van der Waals contribution, is plotted in Fig. 3c. This highlights the significant proportion of the interaction energy originating from dispersive interactions (CH_3CN: 80% at OCP). A Bader charge analysis reports negligible ($\leq|0.05e^-|$) charge transfer between the Au surface and CH_3CN across the modelled potential range (Table S7).[59] With increasingly negative potential, the dispersive interactions, which drive the CH_3CN molecule towards a parallel orientation on the Au surface, are eclipsed by the increasing torque exerted on the molecular dipole moment by the electrode field, allowing the CH_3CN molecule to rotate away from the surface. It should be noted that the polarisation of the interfacial molecules at a charged surface will alter their actual dispersive interactions. Self-consistent treatment of van der Waals interactions in future modelling at applied potential is proposed to improve accuracy – refer to the SI, Note 1.6, for further discussion.

We now turn to bands denoted CN1–3 (Fig. 2). Based on the calculated vibrational wavenumbers of CH_3CN (Fig. 3a), these VSFG bands are unlikely to arise from interfacial CH_3CN. They coincide with the onset of a reductive current observed in the electrochemical data at −0.3 V (Fig. S15–S17), hence we consider reduction products of CH_3CN as assignments. Fig. 3a shows a selection of (scaled) harmonic wavenumbers calculated for breakdown products of CH_3CN at a negatively charged (*ca.* −1.0 V *vs.* SHE) Au(111) surface. The experimental wavenumber of CN2 is in excellent agreement with that calculated for chemisorbed CN^- (CN_{ad}^-) bound atop an Au atom of either the model 111 surface, or an adatom (Fig. 3a). This is in agreement with bands at ∼2130 cm^{-1} assigned elsewhere to CN_{ad}^-.[14,40] For our dry electrolyte experiments, as the intensity of the CN2 band between −0.15 and −0.3 V (Fig. 2a) increases, so do the bands within the CN3 and CN1 regions, hence it seems likely that these bands are related species. CN1 (2175 cm^{-1}) has been observed in other spectroelectrochemical studies of CH_3CN at Au sites, assigned to CN_{ad}^-,[14] or other (non-specified) products of electrochemical reduction of CH_3CN.[40] CN^- adsorption on single-crystal Au electrodes has been studied by IR-visible difference frequency generation spectroscopy, which demonstrated that the potential-dependent wavenumber of CN_{ad}^- is facet-independent.[60] Similarly, a single band assigned to CN_{ad}^- was observed during *in situ* potential-dependent infra-red reflection absorption spectroscopy (IRRAS) of a polycrystalline Au electrode.[61] From these comparisons, bands within the CN3 and CN1 regions are unlikely to be assignable to CN_{ad}^- at different Au sites. Although we note that our Au electrode is nanostructured (Fig. 1c and S20), on similar Au films, only a single band at ∼2124 cm^{-1} (analogous to CN2) is observed in aqueous solutions of KCN, again assigned to CN_{ad}^-.[62]

From the calculated vibrational wavenumbers, CN3 is consistent with ordered CN^- residing within the EDL, not adsorbed to the Au electrode surface denoted CN_{sol}^-. This is in agreement with a previous experimentally determined wavenumber assigned to CN_{sol}^- of 2080 cm^{-1}.[61] Other possible CN-containing species include the organometallic complex $[Au(CN)_2]^-$, observed with a vibrational wavenumber of ∼2146 cm^{-1} and produced during *in situ* IRRAS measurements in aqueous KCN-containing electrolytes at Au electrodes.[61] As this lies between CN1

Open Access Article. Published on 16 December 2025. Downloaded on 5/22/2026 4:03:50 AM. This article is licensed under a Creative Commons Attribution 3.0 Unported Licence.

and CN2, it is an unlikely assignment for the CN1 band. The calculated vibrational wavenumber of $CH_2CN_{ad}^-$ of 2185 cm^{-1} (Fig. 3a) is in excellent agreement with CN1. Alternatively, under anhydrous conditions, CH_3CN undergoes electrochemical reduction to form 3-aminocrotonitrile,[63] with a ν(CN) wavenumber of 2180 cm^{-1}, again in good agreement with the band observed in the CN1 spectral region. Definitive assignment based on a single ν(CN) band is challenging; however, we conclude that several reduction products of CH_3CN have vibrations which lie within the CN1 region. The VSFG spectra obtained before the application of potential in each of the three solvent mixtures are shown in Fig. S8 and S9. In all cases, both CN1 and CN2 bands are observed. Potentially, these species (*e.g.* CN^- or 3-aminocrotonitrile) could be present within the solvent as minor contaminants. In previous spectroelectrochemical studies of the CH_3CN structure at Pt electrodes, CN_{ad}^- is not observed at negative potentials on single crystal Pt,[64] but is observed on highly structured thin films, where it was concluded that the morphology of the electrode surface may play a role in the dissociation of CH_3CN.[36] It has also been suggested that strong plasmonic fields generated during SERS experiments can initiate dissociation,[62,65] deprotonation,[66] and protonation[67] of adsorbed species.

The vibrational wavenumbers of species at electrified interfaces often show potential dependence. This is a result of changing field/surface charge, stability of binding sites, and coverage with applied potential.[8] The intensities of all bands in the undried and wet electrolytes are remarkably similar between +0.3 and −0.15 V, hence we conclude the potential dependence of band wavenumber is controlled by changing interfacial field over this potential range. Tuning rates of adsorbed small molecules, such as CO or CN^-, are often used as indicators of local field strengths,[43,68,69] with the tuning rate of CN2 (CN_{ad}^-) shown in Fig. S4. The tuning rate of CN2 in the dry solvent is obtained after a series of electrochemical measurements were performed as detailed in SI Fig. S18 and S19. From these, relative field strengths obtained are ordered as follows: wet (18 cm^{-1} V^{-1}) > dry (11 cm^{-1} V^{-1}) ≥ undried (7 cm^{-1} V^{-1}). Interestingly, we estimate tuning rates of ∼35 cm^{-1} V^{-1} and ∼40 cm^{-1} V^{-1} when supporting electrolytes containing Li^+ and Na^+ are employed from the CN_{ad}^- band observed in ref. 40, indicating that the local field at the electrode surface is 2.5–3 times smaller when TBA^+ is used as a supporting electrolyte.

It has been shown that for low H_2O concentrations, H_2O can approach the electrode surface without significantly perturbing the CH_3CN structure;[70] however, as the mole fraction of H_2O exceeds ∼0.2, the double-layer capacitance reaches that of aqueous electrolytes, indicating that the EDL is composed of H_2O at the exclusion of CH_3CN.[71] The calculated potential-dependent adsorption energy of a single molecule of water (Fig. 3c, cyan trace) qualitatively supports literature observations that water adsorption at the interface becomes energetically preferable to that of CH_3CN at negative potentials.[70,72] Under anhydrous conditions, the EDL of our negatively charged electrode is expected to consist largely of solvated TBA^+ and free CH_3CN. In the solution phase, the dynamics of CH_3CN molecules are highly correlated, interacting with one another *via* hydrogen bonds, dipole–dipole interactions, and dispersive interactions, forming antiparallel dimers.[73] Gunasekaran and Cuesta assigned bands observed in their SEIRAS spectra of CH_3CN under potential control at an Au electrode to this species.[40] As the CH_3CN antiparallel dimer is centrosymmetric, it would likely not

Open Access Article. Published on 16 December 2025. Downloaded on 5/22/2026 4:03:50 AM.
This article is licensed under a Creative Commons Attribution 3.0 Unported Licence.

be observed in our VSFG spectra unless the structure was significantly perturbed or constrained at the charged interface. In the dry electrolyte, both AN1 and AN2 are barely perceptible. Increasing the H_2O concentration to 2100 ppm, AN2 becomes apparent, and when further increased to 24 000 ppm, both AN1 and AN2 are clearly observed. Consistent with these observations, microstructures of CH_3CN have been shown to be disrupted by H_2O.[74] We hypothesise that at moderate H_2O concentrations (2100 ppm), hydrogen bonding between H_2O and CH_3CN disrupts formation of CH_3CN antiparallel microstructures. This increases the net ordering of CH_3CN at the interface, resulting in an increased AN2 VSFG signal. It has been demonstrated that the addition of (<5%) H_2O to CH_3CN creates a thinner, more compact layer of CH_3CN on single-crystal Pt electrodes.[75] This is in line with the CN_{ad}^- tuning rates obtained in the three electrolytes. We hypothesise that as the H_2O concentration is increased to 24 000 ppm, the disrupted CH_3CN structure, combined with the increased magnitude of E_{DC}, results in increased ordering of CH_3CN further from the electrode surface, giving rise to the greater AN1 VSFG signal. It follows that the H_2O-dependent interfacial structure also stabilises transient interfacial structures differently, resulting in the differing (potential-dependent) intensities of the CN1–3 bands in the VSFG spectra of Fig. 2.

3.2. Effect of NMP on interfacial CH_3CN structure

We turn to investigating the effect of the addition of a non-aqueous co-solvent to the interfacial structure. When adding 10% by volume of (dried) NMP to the (dry) electrolyte solution, we obtain the VSFG spectra shown in Fig. 4a. Residual non-resonant signal is observed at a MIR-NIR delay of 800 fs, and we see no clear CH_3CN bands (AN1/2) above the noise level in these spectra between +0.3 and 0.0 V, although tentatively, bands at ~2225 and ~2250 cm^{-1} may be discerned at negative potentials. No clear resonant signal was observed at an 800 fs MIR-NIR delay in the ν(CO) spectral region (Fig. S12a and S13a). To investigate if potential-dependent changes are occurring that may be hard to observe using the MIR-NIR time-delayed experiment, we have plotted the potential-dependent ratios of the VSFG spectra at a MIR-NIR delay of 0 fs, shown in Fig. 4b and c for the 2000–2300 cm^{-1} and 1550–1850 cm^{-1} regions, respectively. Interpretation of the resonant response in these spectra is complicated as it interferes with the non-resonant response.[56] No clear vibrational bands are observed for AN1/2 but CN_{ad}^- (CN2) is observed in Fig. 4b. In the ν(CO) region, a positive-going band at ~1670 cm^{-1} is observed, increasing in intensity between 0 and −0.45 V (Fig. 4c). This is remarkably similar in wavenumber to the ν(CO) mode of NMP of ~1685 cm^{-1}, observed in the FTIR spectra of the NMP-containing solutions (Fig. S14), hence we assign the VSFG band to this vibration. We are unable to suggest whether the ν(CO) band will appear as a positive or negative feature in the difference spectrum owing to the unknown phases of the contributions to the VSFG signal. The maximum in capacitance of CH_3CN:NMP (9 : 1) $TBAPF_6$ electrolyte at a polycrystalline Au electrode was reported to occur between ~−0.25 and −0.5 V,[21] in excellent agreement with the maximum intensity of the ν(CO) band of Fig. 4c, and is consistent with NMP accumulating at the Au surface between 0 and −0.45 V. At OCP, the adsorption energy of NMP is approximately twice that of CH_3CN (Fig. 3c), indicating that NMP is likely to be adsorbed at this potential.

Open Access Article. Published on 16 December 2025. Downloaded on 5/22/2026 4:03:50 AM.
This article is licensed under a Creative Commons Attribution 3.0 Unported Licence.

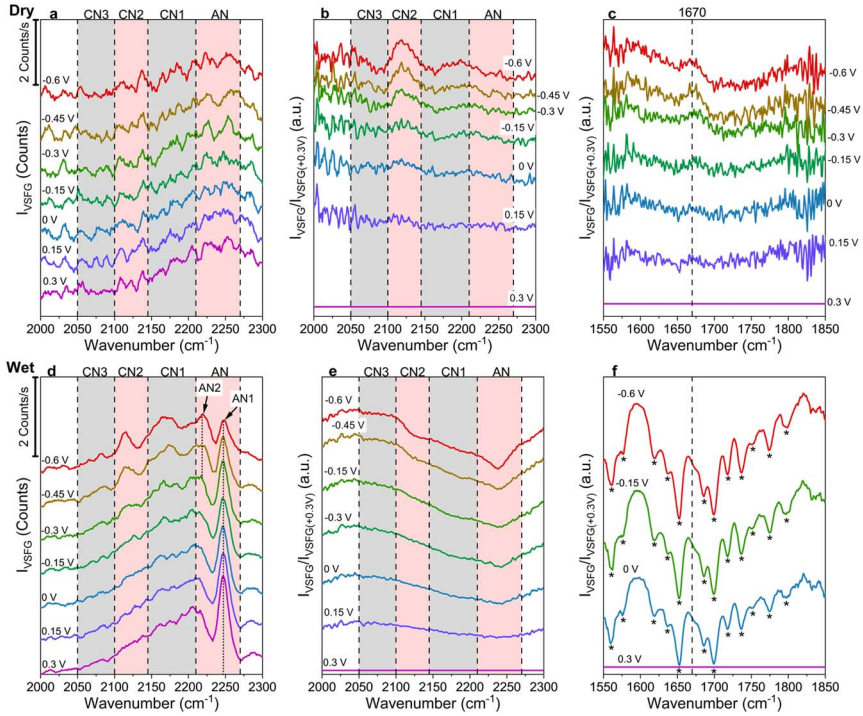

Fig. 4 VSFG spectra for 0.1 M $TBAPF_6$ and 10% NMP acetonitrile: (a–c) dry and (d–e) wet, from data recorded during chronoamperometric measurements going from +0.3 V to −0.6 V *vs.* Ag wire in 0.15 V steps (a–e) or 0.3 V steps (f). Signals in (a) and (d) were taken with an 800 fs delay of the NIR pulse. Signals in (b–f) are obtained from dividing the spectra obtained with a 0 fs MIR-NIR delay at each potential by the spectrum obtained with a 0 fs MIR-NIR delay at +0.3 V *vs.* Ag wire, $I_{VSFG}/I_{VSFG(0.3V)}$. Traces have been offset for clarity. Several spectral regions have been highlighted in parts (a), (b), (d) and (e), denoted as AN, CN1, CN2 and CN3 to facilitate discussion. Asterisks have been added to part (f) to highlight spectral features which are attributable to atmospheric water absorption.

With increasingly negative potential, the adsorption energies of both CH_3CN and NMP decrease; however, NMP is predicted to be more strongly bound at the most negative potential studied in the VSFG experiments.

We also consider the possibility of potential-dependent reorientation of adsorbed NMP. For NMP, we calculate that the torque exerted on the molecular dipole moment by the increasing electrode field is countered by the larger dispersive contribution to the energy. Removing this contribution results in a net energy penalty to adsorption of NMP at a negative potential (Fig. 3c, dashed traces). In determining the orientation and adsorption energy of NMP in our model system, we are limited by the accuracy of our treatment of the dispersive interactions; however, our calculations suggest the NMP orientation shows little potential dependence – refer to Note 1.6 of the SI for further discussion.

Finally, we investigate the wet CH_3CN:NMP electrolyte (25 000 ppm H_2O) (Fig. 4d–f). In the 800 fs delay spectra, AN1 is clearly observed at +0.3 V and decreases in intensity with increasingly negative potential as the CN_{ad}^- (CN2) and AN2 bands increase (Fig. 4d). The clear observance of the AN1/2 bands in the 800

Open Access Article. Published on 16 December 2025. Downloaded on 5/22/2026 4:03:50 AM.
This article is licensed under a Creative Commons Attribution 3.0 Unported Licence.

fs delay spectra in the wet CH_3CN:NMP electrolyte (Fig. 4d) is in stark contrast to the spectra obtained in the dry CH_3CN:NMP electrolyte (Fig. 4a). Spectral changes are also seen in the AN and CN1/2 regions in the 0 fs ratio spectra (Fig. 4e); however, these spectra are difficult to interpret owing to the interference of the resonant and non-resonant contributions to the VSFG signal, which are simplified in the 800 fs delay spectra.[56] Despite this, the clear changes observed in the AN spectral region in the 0 fs ratio spectra of the wet CH_3CN:NMP electrolyte (Fig. 4e) are notably absent in the dry CH_3CN:NMP electrolyte (Fig. 4b). No clear ν(CO) band at $\sim$1670 cm^{-1} is observed, even when the 0 fs ratio spectra are calculated (Fig. 4f). We attribute the broad baseline changes seen in Fig. 4f to the potential-dependent change in non-resonant VSFG signal, while the negative-going sharp features (denoted by asterisks) are determined to be artefacts introduced to the VSFG spectra as a result of absorption of MIR light by residual atmospheric water in the beam path (see Fig. S7). The broad positive-going band between $\sim$1570 and 1620 cm^{-1}, which increases in intensity with increasingly negative potential, is tentatively assigned to the bending mode of H_2O present at the electrode/electrolyte interface. The wavenumber of this mode is dependent on local pH, electrode potential and local solvation structure,[76] making definitive assignment challenging; however, this assignment is consistent with the increased H_2O content of this electrolyte. We conclude that the presence of H_2O disrupts the interfacial NMP structure while increasing CH_3CN ordering, the latter likely to be a result of the same effects described above for the wet CH_3CN electrolyte. A clear negative-going band is observed at $\sim$2235 cm^{-1}, destructively interfering with the residual non-resonant signal in the 800 fs delay spectra (Fig. 4d). The signs of second-order non-linear optical processes are dependent on orientation, although in homodyne VSFG experiments we cannot determine

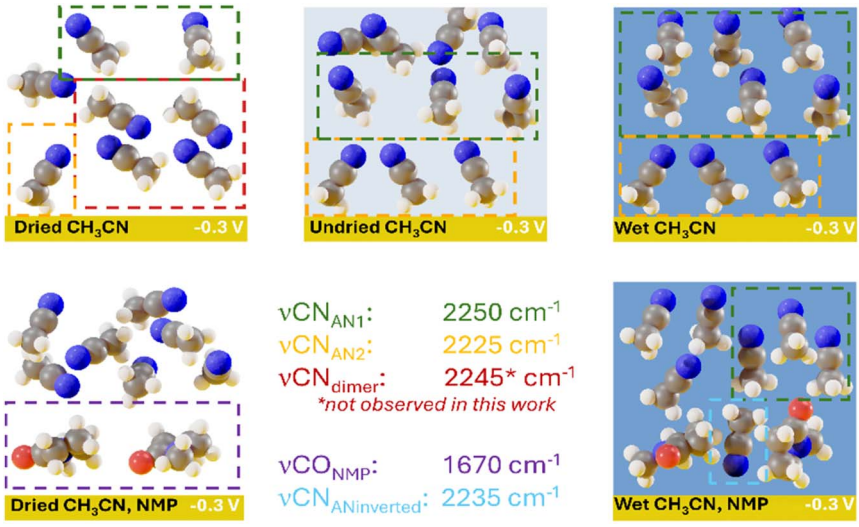

Fig. 5 Schematic representation of the likely orientations of interfacial CH_3CN and NMP at -0.3 V, graphical elements made with VMD and Blender using BlendMol.[77,78] The H_2O orientation is not observed in this work and is represented as the delocalised blue background.

Open Access Article. Published on 16 December 2025. Downloaded on 5/22/2026 4:03:50 AM. This article is licensed under a Creative Commons Attribution 3.0 Unported Licence.

absolute orientation. As CH_3CN species giving rise to the AN1 are not likely to be directly interacting with the Au surface, their orientation is controlled by alignment with E_{DC}, that is, –CN pointing away from the negatively charged Au surface. It follows that the ν(CN) mode of CH_3CN at 2235 cm^{-1} has the opposite orientation (*i.e.*, –CN pointing towards the Au surface). This is not clearly observed in the results of section 3.1. Owing to these comparisons, we conclude that, although not observed directly, NMP resides within the interfacial layer, and driven by intermolecular interactions with NMP and H_2O, a different CH_3CN orientation is formed within the wet NMP electrolyte than in the absence of NMP.

From the results of our combined VSFG and computational study, we summarize the interfacial orientations of CH_3CN and NMP at −0.3 V in Fig. 5.

4. Conclusions

We have shown that the structure of CH_3CN can be studied with VSFG spectroscopy in a "backside" geometry of a thin-film Au electrode. From the results of *ab initio* molecular dynamics, we suggest that CH_3CN molecules directly interacting with the Au electrode have broad vibrational signatures which are redshifted compared to the narrow signatures of the ν(CN) vibration in the bulk. From our computational results, we have been able to rationalise which species are likely to be present at the interface, and their likely potential-dependent orientations. With the inclusion of a moderate concentration of H_2O (2100 ppm), spectral signatures of CH_3CN interacting with the Au surface become increasingly apparent. As the H_2O content is increased further (24 000 ppm), an increase in spectral signatures of CH_3CN close to, but not directly interacting with, the electrode surface is observed in the VSFG spectra. We conclude that the interfacial CH_3CN structure changes with H_2O content *via* two mechanisms: (i) formation of a more compact EDL, increasing the field to which the interfacial species are exposed, and (ii) an increase in the H-bond network between H_2O and CH_3CN disrupting the CH_3CN microstructure. We observed differing intensities of species assigned to dissociation products of CH_3CN at the surface, dependent on both potential and H_2O content, which are likely stabilised to differing extents by these mechanisms. With the addition of NMP to the dry electrolyte, we observed NMP at the negatively charged electrode surface, disrupting the CH_3CN structure. The addition of NMP to the wet electrolyte (25 000 ppm H_2O) results in the absence of any VSFG signature of NMP, but leads to an ordered CH_3CN interfacial layer that differs from the interfacial structure formed in the absence of NMP.

Author contributions

NJDH: investigation, data analysis, writing – original draft, writing – review and editing. COB: investigation, methodology, data analysis, writing – original draft, writing – review and editing. PMD: conceptualization, validation, investigation, supervision, writing – review and editing. HJ: investigation, data analysis, writing – review and editing. BS: validation, writing – review and editing. GT: conceptualization, methodology, supervision, writing – review and editing. AJC: conceptualization, supervision, writing – review and editing, project administration.

 This journal is © The Royal Society of Chemistry 2026

AMG: investigation, conceptualization, methodology, supervision, writing – original draft, writing – review and editing.

Conflicts of interest

There are no conflicts to declare.

Data availability

VSFG spectra and computational geometry files are freely accessible at https://doi.org/10.17638/datacat.liverpool.ac.uk/3055.

Supplementary information (SI): additional discussion regarding experimental procedure, theoretical considerations as well as further electrochemical, spectroscopic and theoretical data to facilitate our discussion. See DOI: https://doi.org/10.1039/d5fd00118h.

Acknowledgements

The EPSRC is acknowledged for the financial support (EP/W038021/1, EP/W033283/1, EP/V011863/2) of H. J., B. S., and A. J. C., while C. O. B. is supported by an STFC-UKRI Ada Lovelace Centre program development studentship. C. O. B. acknowledges access to the STFC SCARF HPC facility. N. J. D. H. is supported through a joint STFC-University of Liverpool Studentship. Thanks are given to Ivan Scivetti (UKRI-STFC) for his implementation of the dispersion correction modifications developed in ref. 49 for VASP 6.x. Thanks are extended to Jon Major for use of the gold evaporator used for electrode synthesis in this work and to Andrea Vezzoli for access to the atomic force microscope used in electrode characterisation. VSFG measurements were performed at the University of Liverpool Early Career Researcher Laser Laboratory supported by UKRI-EPSRC grant EP/S017623/1 and the University of Liverpool, maintained and operated as a shared research facility by the Faculty of Science and Engineering. P. M. D., N. J. D. H. and C. O. B. are grateful for residency at the Research Complex at Harwell.

References

1 S. Chen, Y. Liu and J. Chen, *Chem. Soc. Rev.*, 2014, **43**, 5372–5386.
2 D. G. Nocera, *J. Am. Chem. Soc.*, 2022, **144**, 1069–1081.
3 J. Zhang, Y. Lin and L. Liu, *Phys. Chem. Chem. Phys.*, 2023, **25**, 7106–7119.
4 W. Schmickler, *Chem. Rev.*, 1996, **96**, 3177–3200.
5 C. M. Gunathunge, V. J. Ovalle and M. M. Waegele, *Phys. Chem. Chem. Phys.*, 2017, **19**, 30166–30172.
6 J. Li, X. Li, C. M. Gunathunge and M. M. Waegele, *Proc. Natl. Acad. Sci. U. S. A.*, 2019, **116**, 9220–9229.
7 M. M. Waegele, C. M. Gunathunge, J. Li and X. Li, *J. Chem. Phys.*, 2019, **151**, 160902.
8 J. H. K. Pfisterer, U. E. Zhumaev, W. Cheuquepan, J. M. Feliu and K. F. Domke, *J. Chem. Phys.*, 2018, **150**, 041709.
9 P. B. Joshi, N. Karki and A. J. Wilson, *ACS Energy Lett.*, 2022, **7**, 602–609.

Open Access Article. Published on 16 December 2025. Downloaded on 5/22/2026 4:03:50 AM. This article is licensed under a Creative Commons Attribution 3.0 Unported Licence.

Open Access Article. Published on 16 December 2025. Downloaded on 5/22/2026 4:03:50 AM.
This article is licensed under a Creative Commons Attribution 3.0 Unported Licence.

10 J. A. Rodriguez, C. M. Truong and D. W. Goodman, *J. Chem. Phys.*, 1992, **96**, 7814–7825.
11 B. M. Lindley, A. M. Appel, K. Krogh-Jespersen, J. M. Mayer and A. J. M. Miller, *ACS Energy Lett.*, 2016, **1**, 698–704.
12 R. C. McNulty, K. D. Jones, C. Holc, J. W. Jordan, P. G. Bruce, D. A. Walsh, G. N. Newton, H. W. Lam and L. R. Johnson, *Adv. Energy Mater.*, 2023, **13**, 2300579.
13 V. S. Bryantsev, J. Uddin, V. Giordani, W. Walker, D. Addison and G. V. Chase, *J. Electrochem. Soc.*, 2012, **160**, A160.
14 I. M. Aldous and L. J. Hardwick, *J. Phys. Chem. Lett.*, 2014, **5**, 3924–3930.
15 J.-F. Côté, D. Brouillette, J. E. Desnoyers, J.-F. Rouleau, J.-M. St-Arnaud and G. Perron, *J. Solution Chem.*, 1996, **25**, 1163–1173.
16 E. Pasgreta, R. Puchta, A. Zahl and R. van Eldik, *Eur. J. Inorg. Chem.*, 2007, **2007**, 1815–1822.
17 B. Siritanaratkul, C. Eagle and A. J. Cowan, *Acc. Chem. Res.*, 2022, **55**, 955–965.
18 Q. Zeng, J. Tory and F. Hartl, *Organometallics*, 2014, **33**, 5002–5008.
19 F. Hartl, T. Mahabiersing, S. Chardon-Noblat, P. Da Costa and A. Deronzier, *Inorg. Chem.*, 2004, **43**, 7250–7258.
20 T. Mairegger, H. Li, C. Grießer, D. Winkler, J. Filser, N. G. Hörmann, K. Reuter and J. Kunze-Liebhäuser, *ACS Catal.*, 2023, **13**, 5780–5786.
21 A. M. Gardner, G. Neri, B. Siritanaratkul, H. Jang, K. H. Saeed, P. M. Donaldson and A. J. Cowan, *J. Am. Chem. Soc.*, 2024, **146**, 7130–7134.
22 J. Tory, B. Setterfield-Price, R. A. W. Dryfe and F. Hartl, *ChemElectroChem*, 2015, **2**, 213–217.
23 B. M. Setterfield-Price and R. A. W. Dryfe, *J. Electroanal. Chem.*, 2014, **730**, 48–58.
24 A. V. Rudnev, U. E. Zhumaev, A. Kuzume, S. Vesztergom, J. Furrer, P. Broekmann and T. Wandlowski, *Electrochim. Acta*, 2016, **189**, 38–44.
25 A. J. Wain and M. A. O'Connell, *Adv. Phys.:X*, 2017, **2**, 188–209.
26 L. D. Chen, M. Urushihara, K. Chan and J. K. Nørskov, *ACS Catal.*, 2016, **6**, 7133–7139.
27 S. Ringe, N. G. Hörmann, H. Oberhofer and K. Reuter, *Chem. Rev.*, 2022, **122**, 10777–10820.
28 P. Li, Y. Jiao, J. Huang and S. Chen, *JACS Au*, 2023, **3**, 2640–2659.
29 Y. R. Shen, *Principles of Nonlinear Optics*, Wiley, New York, 1983.
30 A. G. Lambert, P. B. Davies and D. J. Neivandt, *Appl. Spectrosc. Rev.*, 2005, **40**, 103–145.
31 A. M. Gardner, K. H. Saeed and A. J. Cowan, *Phys. Chem. Chem. Phys.*, 2019, **21**, 12067–12086.
32 N. G. Rey and D. D. Dlott, *J. Electroanal. Chem.*, 2017, **800**, 114–125.
33 E. H. G. Backus, N. Garcia-Araez, M. Bonn and H. J. Bakker, *J. Phys. Chem. C*, 2012, **116**, 23351–23361.
34 S. M. Piontek, D. Naujoks, T. Tabassum, M. J. DelloStritto, M. Jaugstetter, P. Hosseini, M. Corva, A. Ludwig, K. Tschulik, M. L. Klein and P. B. Petersen, *ACS Phys. Chem. Au*, 2023, **3**, 119–129.
35 S. Wallentine, S. Bandaranayake, S. Biswas and L. R. Baker, *J. Phys. Chem. A*, 2020, **124**, 8057–8064.
36 A. Sayama, S. Nihonyanagi, Y. Ohshima and T. Tahara, *Phys. Chem. Chem. Phys.*, 2020, **22**, 2580–2589.

 This journal is © The Royal Society of Chemistry 2026

Open Access Article. Published on 16 December 2025. Downloaded on 5/22/2026 4:03:50 AM.
This article is licensed under a Creative Commons Attribution 3.0 Unported Licence.

37 W.-T. Liu and Y. R. Shen, *Proc. Natl. Acad. Sci. U. S. A.*, 2014, **111**, 1293–1297.
38 C. Humbert, T. Noblet, L. Dalstein, B. Busson and G. Barbillon, *Materials*, 2019, **12**, 836.
39 G. Tourillon, L. Dreesen, C. Volcke, Y. Sartenaer, P. A. Thiry and A. Peremans, *Nanotechnology*, 2007, **18**, 415301.
40 P. Gunasekaran and A. Cuesta, *J. Solid State Electrochem.*, 2025, **29**, 2213–2224.
41 P. H. Reinsberg and H. Baltruschat, *Electrochim. Acta*, 2020, **334**, 135609.
42 H. Jang, C. O'Brien, N. J. D. Hill, A. M. Gardner, I. Scivetti, G. Teobaldi and A. J. Cowan, *ACS Catal.*, 2025, **15**, 11452–11462.
43 L. C. Banerji, H. Jang, A. M. Gardner and A. J. Cowan, *Chem. Sci.*, 2024, **15**, 2889–2897.
44 G. Kresse and J. Furthmüller, *Phys. Rev. B:Condens. Matter Mater. Phys.*, 1996, **54**, 11169–11186.
45 G. Kresse and D. Joubert, *Phys. Rev. B:Condens. Matter Mater. Phys.*, 1999, **59**, 1758–1775.
46 S. M. R. Islam, F. Khezeli, S. Ringe and C. Plaisance, *J. Chem. Phys.*, 2023, **159**, 234117.
47 J. P. Perdew, K. Burke and M. Ernzerhof, *Phys. Rev. Lett.*, 1996, **77**, 3865–3868.
48 S. Grimme, *J. Comput. Chem.*, 2006, **27**, 1787–1799.
49 S. Sakong and A. Groß, *ACS Catal.*, 2016, **6**, 5575–5586.
50 S. Nosé, *J. Chem. Phys.*, 1984, **81**, 511–519.
51 D. West and S. K. Estreicher, *Phys. Rev. Lett.*, 2006, **96**, 115504.
52 M. Brehm and B. Kirchner, *J. Chem. Inf. Model.*, 2011, **51**, 2007–2023.
53 M. Brehm, M. Thomas, S. Gehrke and B. Kirchner, *J. Chem. Phys.*, 2020, **152**, 164105.
54 M. Thomas, M. Brehm, R. Fligg, P. Vöhringer and B. Kirchner, *Phys. Chem. Chem. Phys.*, 2013, **15**, 6608–6622.
55 A. Hjorth Larsen, J. Jørgen Mortensen, J. Blomqvist, I. E. Castelli, R. Christensen, M. Dułak, J. Friis, M. N. Groves, B. Hammer, C. Hargus, E. D. Hermes, P. C. Jennings, P. Bjerre Jensen, J. Kermode, J. R. Kitchin, E. Leonhard Kolsbjerg, J. Kubal, K. Kaasbjerg, S. Lysgaard, J. Bergmann Maronsson, T. Maxson, T. Olsen, L. Pastewka, A. Peterson, C. Rostgaard, J. Schiøtz, O. Schütt, M. Strange, K. S. Thygesen, T. Vegge, L. Vilhelmsen, M. Walter, Z. Zeng and K. W. Jacobsen, *J. Phys.: Condens. Matter*, 2017, **29**, 273002.
56 A. Lagutchev, S. A. Hambir and D. D. Dlott, *J. Phys. Chem. C*, 2007, **111**, 13645–13647.
57 B. Dereka, N. H. C. Lewis, J. H. Keim, S. A. Snyder and A. Tokmakoff, *J. Phys. Chem. B*, 2022, **126**, 278–291.
58 Q. Yang and J. Bloino, *J. Phys. Chem. A*, 2022, **126**, 9276–9302.
59 W. Tang, E. Sanville and G. Henkelman, *J. Phys.:Condens. Matter*, 2009, **21**, 084204.
60 A. Le Rille, A. Tadjeddine, W. Q. Zheng and A. Peremans, *Chem. Phys. Lett.*, 1997, **271**, 95–100.
61 K. Kunimatsu, H. Seki, W. G. Golden, J. G. Gordon and M. R. Philpott, *Langmuir*, 1988, **4**, 337–341.
62 D. Shin, *Spectrochim. Acta, Part A*, 2021, **263**, 120191.
63 J. K. Foley, C. Korzeniewski and S. Pons, *Can. J. Chem.*, 1988, **66**, 201–206.

Open Access Article. Published on 16 December 2025. Downloaded on 5/22/2026 4:03:50 AM.
This article is licensed under a Creative Commons Attribution 3.0 Unported Licence.

64 S. Baldelli, G. Mailhot, P. Ross, Y.-R. Shen and G. A. Somorjai, *J. Phys. Chem. B*, 2001, **105**, 654–662.
65 W.-S. Zhang, Z.-F. Zhang and Z.-L. Zhang, *J. Electroanal. Chem.*, 2002, **528**, 1–17.
66 P. Singh, T. Deckert-Gaudig, Z. Zhang and V. Deckert, *Analyst*, 2020, **145**, 2106–2110.
67 P. Singh and V. Deckert, *Chem. Commun.*, 2014, **50**, 11204–11207.
68 J. A. Rebstock, Q. Zhu and L. R. Baker, *Chem. Sci.*, 2022, **13**, 7634–7643.
69 S. D. Fried and S. G. Boxer, *Acc. Chem. Res.*, 2015, **48**, 998–1006.
70 C. Deacon-Price, N. Chen, A. Lal, P. Broersen, E. J. Meijer and A. C. Garcia, *ChemCatChem*, 2025, **17**, e202401332.
71 K. J. Aoki, J. Chen and P. Tang, *Electroanalysis*, 2018, **30**, 1634–1641.
72 S. Baldelli, G. Mailhot, P. N. Ross and G. A. Somorjai, *J. Am. Chem. Soc.*, 2001, **123**, 7697–7702.
73 V. A. Koverga, O. M. Korsun, O. N. Kalugin, B. A. Marekha and A. Idrissi, *J. Mol. Liq.*, 2017, **233**, 251–261.
74 T. V. Bogdan, A. A. Firsov, V. P. Chertkova and A. I. Abramovich, *J. Struct. Chem.*, 2024, **65**, 2153–2162.
75 S. Baldelli, N. Markovic, P. Ross, Y.-R. Shen and G. Somorjai, *J. Phys. Chem. B*, 1999, **103**, 8920–8925.
76 M. Dunwell, Y. Yan and B. Xu, *Surf. Sci.*, 2016, **650**, 51–56.
77 W. Humphrey, A. Dalke and K. Schulten, *J. Mol. Graphics*, 1996, **14**, 33–38.
78 J. D. Durrant, *Bioinformatics*, 2018, **35**, 2323–2325.

 This journal is © The Royal Society of Chemistry 2026